Plasma Processes and Polymers

PLASMA PROCESSES AND POLYMERS

RESEARCH ARTICLE OPEN ACCESS

Ammonia to Hydrogen Conversion in a Ferroelectric Packed-Bed Plasma Reactor: The Effect of a High-Permittivity Effective Medium Material

Paula Navascués[1] | Mateo Ruiz-Martín[1,2] | Guillermo Regodón[1] | Alberto Palmero[1] | J. Cotrino[1,2] | Agustín Rodríguez González-Elipe[1] | Ana Gómez-Ramírez[1,2]

[1]Laboratory of Nanotechnology on Surfaces and Plasma, Instituto de Ciencia de Materiales de Sevilla (CSIC-Universidad de Sevilla), Seville, Spain | [2]Departamento de Física Atómica, Molecular y Nuclear, Universidad de Sevilla, Seville, Spain

Correspondence: Paula Navascués (paula.navascues@icmse.csic.es) | Ana Gómez-Ramírez (anamgr@us.es)

Received: 5 May 2025 | **Revised:** 11 July 2025 | **Accepted:** 16 July 2025

Keywords: ammonia | ferroelectrics | hydrogen | packed-bed plasma reactor | plasma-catalysis

ABSTRACT

Herein we report about the ammonia to hydrogen conversion induced at ambient conditions in a ferroelectric barrier discharge plasma. Decomposition yields of 40% have been found at 2.5 kV of applied voltage in a packed-bed reactor moderated with ferroelectric PZT pellets, bared and coated with layers of agglomerated Al_2O_3 and Ru/Al_2O_3 powders. The electrical analysis of plasma discharges, their modeling within an equivalent circuit approach and their optical emission spectroscopy characterization suggest that conventional catalytic contributions to reaction yield are negligible, even with Ru/Al_2O_3 coated pellets for which a maximum decomposition yield was found. We propose that the main function of the Ru/Al_2O_3 coating is to act as a high permittivity effective medium material enhancing plasma current and hence conversion yield.

1 | Introduction

More than a century after the development of the Haber-Bosch process, the easier handling and transportation of ammonia with respect to hydrogen has fostered a so-called second ammonia revolution centered on the use of ammonia as a hydrogen vector to feed fuel cells and other devices [1]. A key issue for these applications is the in-situ decomposition of ammonia, customarily referred to as *ammonia to hydrogen*.

The ammonia decomposition process is typically performed at high temperatures [2] with the aid of catalysts based on metals such as ruthenium, iron, or nickel [3, 4]. These thermo-catalytic processes usually proceed in large reactors, require long induction periods to reach steady state conditions, and are unsuitable for intermittent low-temperature operation [3]. Reducing reactor size and decreasing the stabilization times are additional requirements for an efficient use of the *ammonia to hydrogen* technology in a distributed way (i.e., in processes based on small production plants connected with the electricity grid). Electricity driven plasma-catalysis processes comply with these conditions as they operate on small scales at ambient or mild temperatures and require a practically zero induction time.

First studies about ammonia decomposition using plasmas were reported in the second half of the past century, using glow [5] and radiofrequency (RF) discharges [6, 7] at low pressures, in investigations that had an academic character. It has been only recently realized that, in parallel to studies about the synthesis of ammonia at higher pressures [8–10], plasma decomposition of this compound is highly relevant for the production of hydrogen [11–14]. Plasma *ammonia to hydrogen* processes,

Current Addresses: Paula de Navascues: Laboratory for Advanced Fibers, Empa, Swiss Federal Laboratories for Materials Science and Technology, Lerchenfeldstrasse 5, St. Gallen 9014, Switzerland. Guillermo Regodon: Departamento de Física, Campus Universitario de Rabanales, Universidad de Córdoba, Córdoba 14071, Spain.

following an in-plasma catalysis approach [15], have been carried out at atmospheric [16, 17] and reduced [18] pressures using microwave (MW), gliding arc [19–22], or dielectric barrier discharge (DBD) packed-bed reactors [8–10, 23–30]. Using this latter approach with different catalysts and pure ammonia flows, L. Wang and collaborators reported decomposition yields higher than 15% at 300°C that amounted to ca. 99% at 410°C [25–27]. Andersen et al. reported a decomposition yield of 12.6% for a packed-bed reactor filled with $MgAl_2O_3$ pellets [29]. Furthermore, studies by Hayakawa et al. proved the relevance of incorporating hydrogen selective membranes into packed-bed reactors, obtaining decomposition yields of 24% at room temperature [28]. Higher ammonia decomposition yields have been reported by other authors, but in many cases working at high temperatures [22–24, 27, 31] or at room temperature with ammonia diluted in inert carrier gases [8, 10]. For example, Y. Gao et al. recently reported 100% of ammonia decomposition using $FeCo/CeO_2$ nanospheres at 550°C and a 5% NH_3/Ar mixture [31].

Herein, we investigate the effect of incorporating a ruthenium catalyst into the *ammonia to hydrogen* process in a packed-bed plasma reactor. The packed-bed consisted of ferroelectric PZT (lead zirconate titanate) pellets acting as discharge moderators. From now on this configuration will be designated as ferroelectric barrier discharge, FBD [32]. This type of reactor operates at lower voltages than common DBD reactors, resulting in relatively lower power consumptions, i.e., a promising trade-off between reaction yield and energy efficiency for plasma-assisted reactions [33, 34]. In this study, coated ferroelectric pellets were introduced in the center of the packed barrier, incorporating agglomerated powders of either alumina or alumina-supported ruthenium. The studied distributions of pellets are referred to as PZT (bare ferroelectric barrier), Al_2O_3/PZT (incorporating only the alumina support) and Ru-Al_2O_3/PZT (incorporating the alumina support and ruthenium) reactor configurations. These barriers have been previously tested by our group for the synthesis of ammonia using N_2/H_2 mixtures [35]. The reaction mechanisms have been analyzed by optical emission spectroscopy (OES) to determine possible effects of the barriers and Ru nanoparticles in the process. The results showcase that PZT-moderated FBD reactors efficiently decompose ammonia at ambient conditions, and that the reaction yield increases when using metal-dielectric layers (i.e., Ru-Al_2O_3) as coatings for the ferroelectric pellets.

2 | Materials and Methods

2.1 | Ferroelectric Packed-Bed Plasma Reactor, Electrical Characterization, and Reaction Efficiency

Experiments were carried out at room temperature and atmospheric pressure in a packed-bed plasma reactor with a parallel-plate geometry, with electrodes separated by a 5 mm gap. Figure 1 illustrates a sketch of the packed-bed reactor and its connection with the power supply and the analytical systems. Experiments were performed at a fixed operating frequency of 5 kHz and high voltage was applied in the range of 1.0 to 2.5 kV. The applied voltage served as a control parameter to adjust the electric field distribution between the electrodes and, hence, the energy of plasma electrons. Analytical techniques include Optical Emission Spectroscopy (OES), Electrical Characterization, and Quadrupole Mass Spectrometry (QMS). The OES spectra were acquired with a Horiba monochromator (Jobin Yvon FHR640) equipped with a diffraction grating with a density of 1201 lines/cm, centered at 330 nm, and measuring with a resolution of 0.5 nm and an integration time of 1 s. The *I (t)* and *V(t)* characteristic curves were determined by means of a current monitor (Pearson, 6585) located after the reactor and a high voltage probe integrated into the power supply, respectively. A 2.51μF-capacitor located between the reactor and the ground was used to determine the transferred charge and, from it and the applied voltage, the average consumed power, this latter estimated from the area of the monitored Lissajous plots [36]. For the mass spectrometry analysis, a quadrupole mass spectrometer (Pfeiffer Vacuum, QMG 220 Prisma Plus) was used. The ferroelectric material used as discharge moderator (i.e., barrier material) was lead zirconate titanate (PZT). PZT pellets were prepared by sintering powders of this material supplied by APC International Ltd. (US) as described in the reference [37]. The PZT beads have sizes in the range of 0.5–2 mm. Ru-Al_2O_3 (0.9 wt% Ru) or Al_2O_3-coated PZT pellets with an average diameter of 1.25 mm were prepared as reported in Supplementary Material S1 following a typical wet impregnation method. The packed bed barrier consisted of three

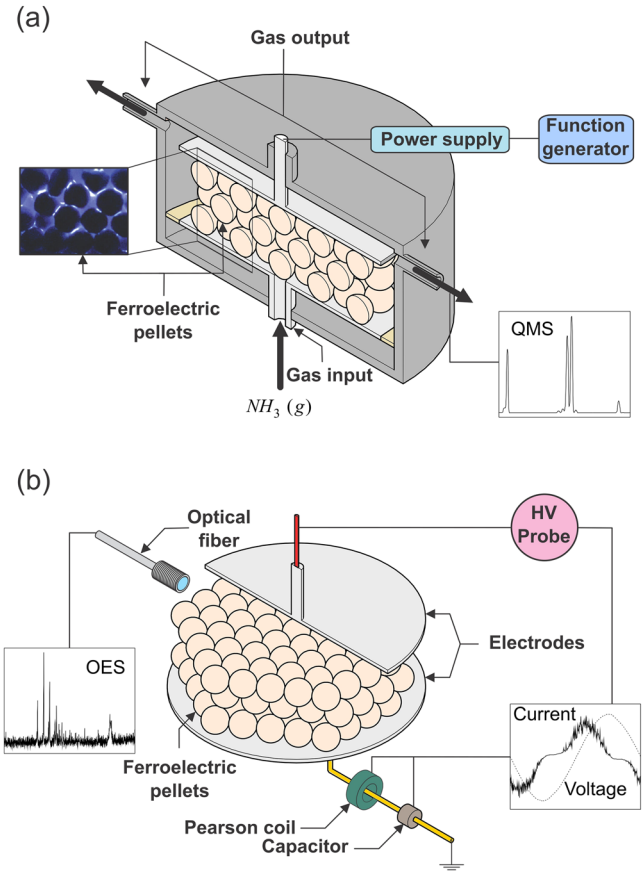

FIGURE 1 | (a) Sketch of the reaction system (packed-bed reactor & electrical excitation system). (b) Experimental setup indicating the connections between the gas supply, the reactor, and the analytical system used.

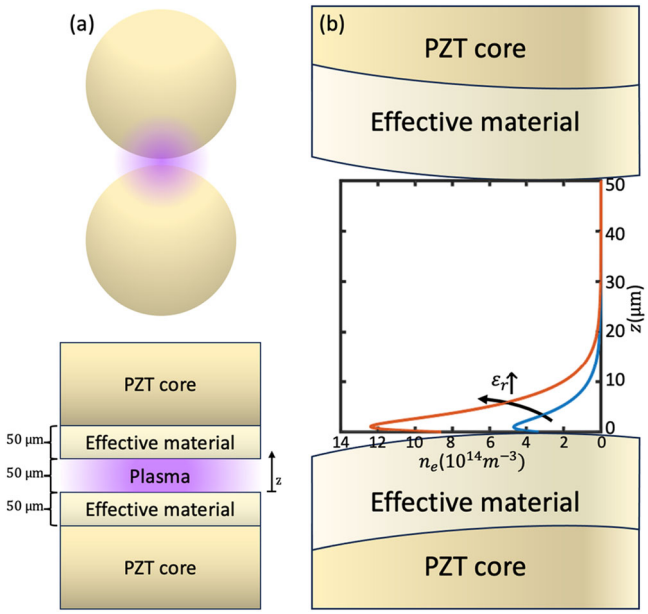

FIGURE 2 | (a) Diagram of the geometry used for the simulations, (b) Evolution of the electron density across the interelectrode gap for increasing values of the permittivity of the coating layer on the pellet. Blue and red curves correspond to the calculations carried out for the permittivity values assumed for Al_2O_3 and Ru-Al_2O_3 coatings, respectively. Simulations correspond to a difference of voltage of 750 V between pellets.

sandwiched layers of piezoelectric pellets: PZT/PZT/PZT, PZT/Al_2O_3-PZT/PZT, and PZT/Ru-Al_2O_3-PZT/PZT, the central layer defining the three investigated reactor configurations (PZT, Al_2O_3/PZT and Ru-Al_2O_3/PZT). This specific distribution of pellets was chosen to prevent direct contact between the metal nanoparticles and the electrodes, which could result in short circuits hazards when using Ru-Al_2O_3/PZT pellets. For more details on the experimental configuration, we refer the reader to our previous publication [35]. To ignite the discharge, high voltage sinusoidal signals were applied between the electrodes by means of a function generator (Stanford Research Systems, Model DS345) connected to an amplifier (Trek Inc. Model PD05034).

The NH_3 was introduced into the reactor through a hole located in the center of the bottom electrode, while the outlet gas mixture left the reactor chamber through two exhaust tubes located in the upper part. The gas flow rate was monitored with mass flow controllers (MFC, Bronkhorst, Netherlands). Pure-ammonia discharges were ignited for an input flow rate of 9 sccm.

To evaluate the performance of the process we used the decomposition yield and the energy efficiency as key parameters. The decomposition yield, DY_{NH3} [%] is defined as:

$$DY_{NH_3}[\%] = \frac{M_{NH_3}(\text{in})\,[\text{sccm}] - M_{NH_3}(\text{out})\,[\text{sccm}]}{M_{NH_3}(\text{in})\,[\text{sccm}]} \cdot 100 \quad \text{(E1)}$$

where M_{NH3} (in) and M_{NH3} (out) refer to the inlet and outlet ammonia flows, respectively. We also evaluate the energy efficiency for H_2 production, EE-H_2 [LH_2/kWh] defined as:

$$EE{-}H_2\,[LH_2{\cdot}(kWh)^{-1}] = \frac{V_{H_2}(\text{out})\,[\text{sccm}]{\cdot}60\,[\text{min}{\cdot}\text{h}^{-1}]}{\text{Power}\,[\text{kW}]} \quad \text{(E2)}$$

where V_{H2} (out) refers to the volume (in liters) of H_2 that is produced by the decomposition of ammonia.

The electrical behavior of the packed-bed reactor in the absence of plasma for the PZT, Al_2O_3/PZT and Ru-Al_2O_3/PZT configurations was characterized by means of impedance spectroscopy using an AUTOLAB 302 N potentiostat/galvanostat combined with a FRA32M module [32]. The measurements were carried out in the absence of plasma, but after having performed the plasma experiments, i.e., to determine the electrical characteristics of the reactor once steady state conditions had been reached during plasma activation. As a result of this characterization, specific Nyquist plots were obtained for the three investigated configurations of the reactor.

2.2 | Characterization of Powders Used to Coat the Pellets

As described in the previous section, the pellets used to build the ferroelectric barrier consisted of bare PZT ferroelectric pellets, as well as pellets coated with Al_2O_3 or Ru-Al_2O_3 powders. These powders were characterized by means of transmission electron microscopy, scanning electron microscopy (equipped with an energy-dispersive X-ray analyzer), and X-ray photoelectron spectroscopy. The characterization of the material has already been published in a previous work dedicated to ammonia synthesis [35], and we refer the reader to this study. EDX, SEM, and TEM analysis of the Al_2O_3 and Ru-Al_2O_3 powders showed that Ru is dispersed within the Al_2O_3 phase, forming aggregates of Ru nanoparticles with an average size of 120 nm. XPS analysis corroborated these results and allowed estimating the concentration of Ru at the surface of the powder as around 0.9 wt%.

Coated ferroelectric pellets were analyzed with the same techniques. The details of this characterization are also provided in the reference [35], but it is worth mentioning that coatings were not fully conformal and that a minor part of the surface of some PZT pellets might be uncoated with Al_2O_3 or Ru-Al_2O_3 powders. Results also confirmed that Ru is dispersed homogeneously in the pores of the alumina, although, as mentioned earlier, it may aggregate in the form of nanoparticles and small agglomerates. This distribution allows us to treat the coatings as an effective metal-dielectric medium (Ru-Al_2O_3) where Ru particles are not only on the outer surface of the coating but also inside. As demonstrated in subsequent sections, the high dielectric constant of this effective medium contributes to enhance the plasma intensity in the packed-bed reactor.

2.3 | COMSOL Multiphysics® Simulation of Interpellet Plasma Discharge

The COMSOL Multiphysics® [38] simulation implemented in this work is a variation of the well-established 1D-DBD

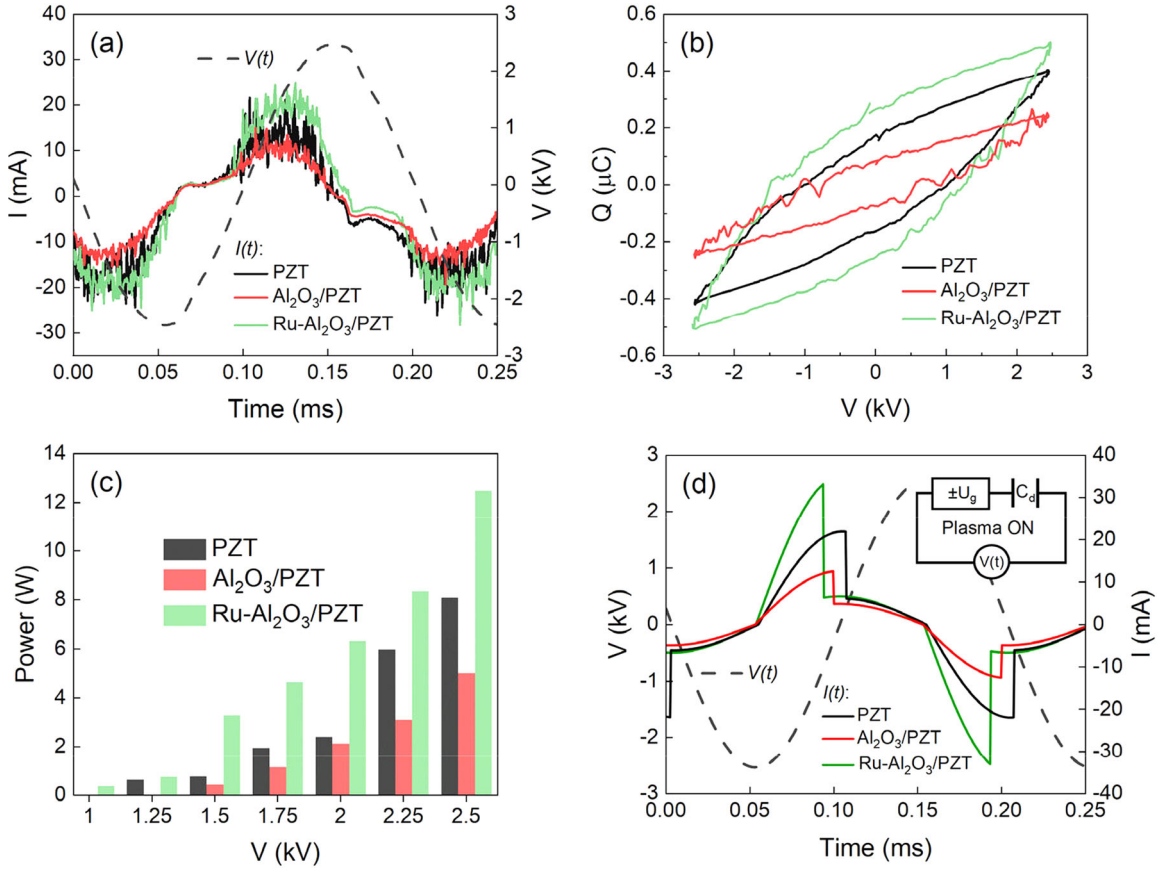

FIGURE 3 | Electrical characterization and simulation of the plasma for the utilized rector configurations. (a) *V(t)* and *I(t)* plots. (b) Lissajous curves. (c) Power consumed by the reactor as a function of the applied voltage. (d) Theoretically calculated *I(t)* curves for the equivalent circuit employed to simulate the reactor, which is included as an inset.

simulation of an argon plasma [39, 40]. This simulation was carried out to gain insight into the effect of ruthenium particles onto the electron density, assuming these particles are distributed within the coating of the pellets and that such coating can be treated in the simulation as an effective medium. As previously mentioned, our goal is to comparatively assess the influence of this Ru-containing coating on the plasma electron density. Therefore, for the sake of simplicity, an argon plasma was used for this purpose. To obtain the electron density in the inter-pellet region, we model the discharge in a small gap (50 μm) assuming a planar geometry, as schematically represented in Figure 2a. A coating thickness of 50 μm was assumed. The dielectric permittivity for the materials forming part of the bed was taken as 1704.4 for PZT, 11.54 for Al_2O_3, both obtained from the COMSOL Multiphysics® materials reference, and 23.08 for the Ru/Al_2O_3 coating. This value of dielectric permittivity has been taken from reference [41] and correspond to Fe/Al_2O_3 composite, with a metal phase content of 3% in mass percentage/1.5% in volume percentage, values in the order of magnitude expected for the Ru/Al_2O_3 powder. Ceramic-metal composites are known by their high permittivity and the ratio ceramic/metal and the distribution of the latter in the matrix are key issues for the control of this parameter [42, 43]. The AC voltage drop across the inter-pellet distance was chosen as a 750 V, varying with a frequency of 5 kHz and a sinusoidal profile. The voltage amplitude was chosen because it is close to one-third of the DBD voltage (2.5 kV) used in the experiments where the bed is formed by three layers of pellets defining four air gaps from the ground bottom to the active top electrode, Assuming that the voltage drop will be very small through the fourth air gap existing between the pellets and the ground electrode, it is a reasonable assumption that the applied voltage distributes rather homogeneously between the other three gaps.

For the simulations carried out in this study, the imaginary part of the dielectric permittivity is neglected due to the low frequency used in our experiments, i.e., 5 kHz. This assumption stems from the results of Shi et al. 2014 [41], and takes into account the low ruthenium volume percentage used in this study. For the calculations, we assume a time-dependent 1D plasma system, which is iteratively solved until a stationary result is found. Then, the concentrations of the ions, electrons and neutral species are determined as in reference [44].

3 | Results and Discussion

3.1 | Electrical Characterization

To analyze the effect of the electrical characteristics of the coatings (i.e., their permittivity) and the electron density, we have conducted COMSOL Multiphysics® simulations to assess the evolution of plasma density between two adjacent PZT pellets covered with either Al_2O_3 or $Ru\text{-}Al_2O_3$ coatings (50 μm thickness) for a voltage difference between pellets of 750 V, as schematically represented in Figure 2a.

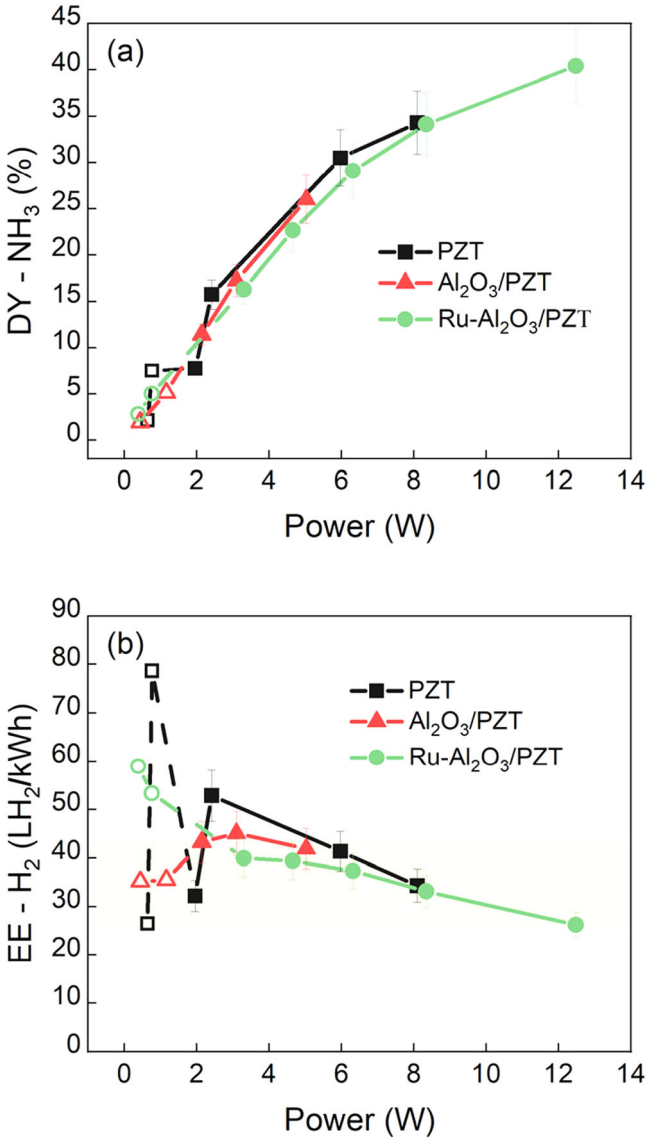

FIGURE 4 | Evolution with respect to the power of (a) decomposition yield and (b) energy efficiency of the *ammonia to hydrogen* reaction at room temperature for the three reactor configurations. The yellow band in (b) highlights that efficiency is similar for the three reactor configurations for decomposition yields higher than 5%. Note that the zone of the curves corresponding to low values of decomposition yield that were subjected to high uncertainties are plotted with dashed lines and empty dots. The power values correspond to applied voltages ranging between 1.0-2.5 kV.

The PZT core of the pellets is assumed to have constant potential. In DBD, this approximation has been shown to be valid for electromagnetic simulations of the full packed bed [45, 46]. By the 1D-DBD planar geometry simulations carried out here we consider different situations in the region between the two PZT cores. Namely, we consider that the coatings on two opposed pellets act as effective medium materials characterized with specific dielectric properties. The permittivity of the coating on the pellets was systematically varied from the value used for alumina to that assumed for Ru-Al_2O_3 (see the Materials and Methods section). The profiles of plasma density curves along the interpellet gap space were then estimated as shown in Figure 2b for Al_2O_3 -blue curve- and Ru-Al_2O_3 -red curve- (note that the plasma density curves are plotted at the instant when the plasma density reaches a maximum value during an AC cycle). It is apparent that the higher permittivity values used for the simulation of the plasma, the higher the obtained electron density values. Furthermore, the maximum electron density increased with voltage, as expected, for both electrical permittivity values (see Supplementary Material S2). As it will be shown below, this result is consistent with the experiments and supports that a coating behaving as an effective medium with a higher electrical permittivity leads to an increase in plasma density across the inter-pellet region.

The simulation analysis of the effect of pellet coatings on the density of plasmas was confirmed experimentally. Figure 3a shows the *I(t)* curves recorded upon plasma ignition for the different reactor configurations at 2.5 kV. The amplitude of current curves follows the order Ru-Al_2O_3/PZT > PZT> Al_2O_3/PZT. The Lissajous curves (*Q*–*V* plots) in Figure 3b derived from these plots clearly visualize the differences in the amount of electric charge exchanged during operation with these three barriers. Data in these figures show that the Al_2O_3 coating decreases the current, while the Ru-Al_2O_3 coating enhances plasma current. A similar result has been previously reported for FBD plasmas intended to induce the ammonia synthesis reaction from pure $N_2 + H_2$ mixtures [35]. The evolution of power with the applied voltage confirms the found tendency for the three configurations (c.f. Figure 3c). Both the Lissajous curves and the power plots as a function of the voltage support that plasma responds differently to the electrical characteristics of the barrier. It is noteworthy in this regard that in the absence of plasma, the electrical features of the reactor varied with the type of barrier as determined by impedance electrical spectroscopy analysis [32], (see *Nyquist* plots Supplementary Material S3).

The electrical behavior of plasma discharges in DBD reactors is usually described using equivalent circuits as that depicted in the inset in Figure 3d for plasma -on states [36]. Based on this equivalent circuit model, we have calculated the capacitance of the barrier (C_{diel}) and the plasma current for the three configurations (see details of this analysis in the Supplementary Material S4). The calculated curves shown in Figure 3d indicate that the intensity jumps in *I(t)* follow the same trend than the experimentally determined intensity of microdischarges (c.f., Figure 3a). These calculations and the electrical evaluation of plasma current indicate that the higher value of this magnitude experimentally obtained for the Ru-Al_2O_3/PZT configuration can be associated with a higher value of C_{diel} in this case. This agress with the already enunciated thesis that the Ru-Al_2O_3 coating behaves as an effective metal-dielectric medium characterized by a higher permittivity than that of the pure Al_2O_3 coating (a similar electrical behavior is well-known for metal-dielectric composites characterized by a high value of permittivity [42, 43]).

3.2 | Efficiency of Ammonia Decomposition Reaction

Pure NH_3 discharges were ignited at room temperature for the electrical operation conditions described above. Experiments

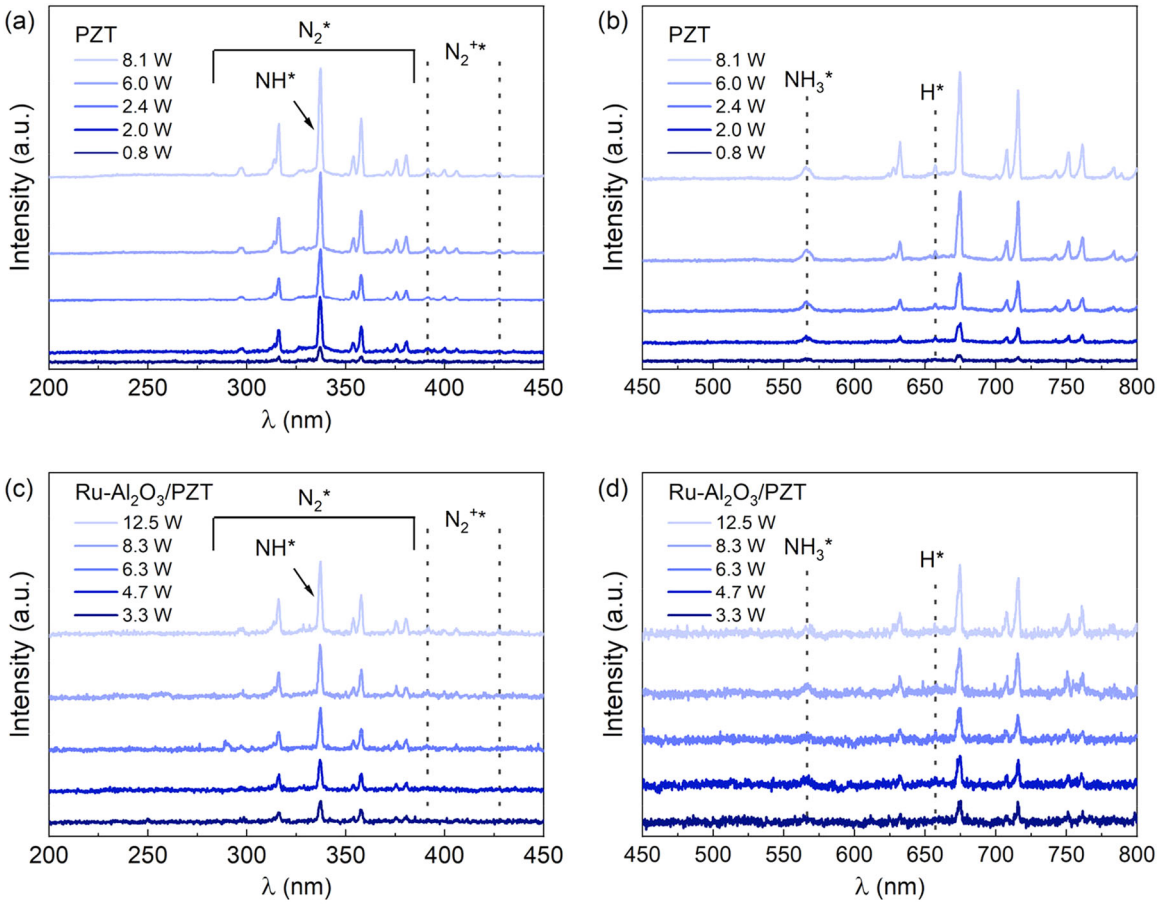

FIGURE 5 | OES spectra for different consumed powers for the (a,c) 200–450 nm region and (b,d) the 450–800 nm region. Data acquired for the (a,b) PZT and (c,d) Ru-Al_2O_3/PZT configurations. The indicated power values correspond to applied voltages within a range between 1.0 and 2.5 kV for both reactor configurations.

showed that plasma decomposition of pure ammonia rendered N_2 and H_2 with no signs of hydrazine (see Supplementary Material S5), results thar are in line with other DBD atmospheric-pressure plasma experiments [8, 20, 21, 29]. Results for FBD *ammonia to hydrogen* conversion are shown in Figure 4. Figure 4a and b show that decomposition rate and energy efficiency for hydrogen production increase with power for the three reactor configurations in a similar way. A maximum decomposition yield of 40% was achieved for the Ru-Al_2O_3/PZT configuration, of 34% for PZT, and of 26% for the Al_2O_3/PZT configuration. This is so because for a given voltage, the Ru-Al_2O_3/PZT configuration delivers a higher current, resulting in higher power and, consequently, greater decomposition yields. The energy efficiencies as a function of power (c.f., Figure 4b) varied between 25 and 55 LH_2/kWh and followed a similar decreasing tendency for the three cases when the power was higher than 2W, i.e., when decomposition yield is high enough to discard large errors and therefore a sound calculation of the EE. We emphasize that the similar evolution of decomposition rate and energy efficiency as a function of power found for the three configurations supports that the total current is the main factor controlling the *ammonia to hydrogen* decomposition process. The higher decomposition yield in the presence of Ru agrees with results by El-Shafie et al. i.e., showing that the addition of Ru particles to a packed-bed reactor produced an increase in the ammonia decomposition yield with respect to that in a standard (in case of these authors, SiO_2) dielectric packed-bed [30]. However, whether the observed increases are due to catalytic effects driven by the ruthenium is a question of debate [35, 47, 48], as indicated by the results in the present work evidencing the higher intensity of the plasma when the Ru-Al_2O_3/coating covers the PZT pellets (c.f., Figure 3).

3.3 | Optical Emission Characterization and Reaction Mechanisms

To gain insights into the reaction mechanisms, NH_3 discharges were analyzed using OES for the PZT, Al_2O_3/PZT and the Ru-Al_2O_3/PZT configurations (see a set of emission spectra in the 240–450 nm range **in** Supplementary Material S6). This technique permits detecting plasma excited species [49] and to compare their relative populations [33]. Figure 5 shows steady-state OES spectra for the 200-450 nm region (Figure 5a,c) and for the 450-800 nm region (Figure 5b,d) recorded for the PZT and Ru-Al_2O_3/PZT configurations at different powers. These measurements were carried out once the reactor reaches steady-state conditions and therefore the concentration of excited species derived from ammonia and the resulting reaction products do not change over time. The 200–450 nm spectra in Figure 5a,c depict characteristic bands of NH* (transition

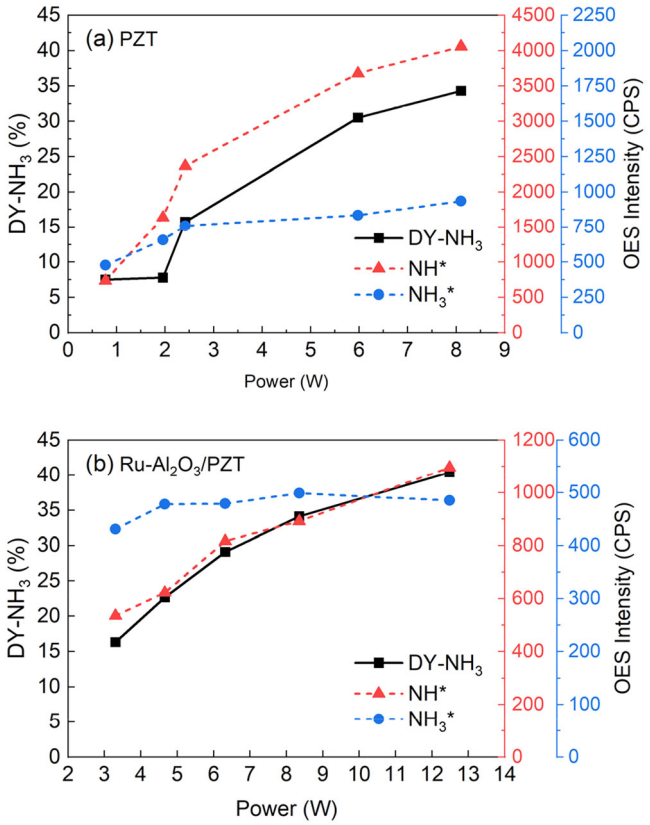

FIGURE 6 | Decomposition yield (square dots, black line), NH* emission intensity (triangle dots, red dashed line), and NH_3* emission intensity (circle dots, blue dashed line) as a function of power for (a) PZT and (b) Ru-Al_2O_3/PZT configurations. Note the different scales used to represent the emission intensity of the NH* and NH_3* bands.

$[A^3\Pi \rightarrow X^3\Sigma^-]$), N_2 (second positive system), and N_2^+* (first negative system) species. These bands can be also followed during the ammonia synthesis reaction [33, 50]. The 450–800 nm NH_3* Schuster's bands shown in Figure 5b,d appear between 564 and 567 nm [11], while a little H_α line appears at 656.3 nm [52]. Bands between 560 and 900 nm are second order N_2-bands.

In previous studies, the formation of NH* species has been attributed to plasma processes resulting from the interaction of plasma electrons with ammonia molecules. It has been also assumed that these species were involved in the decomposition of NH_3 [50, 51]. On the other hand, working with a Fe-based catalyst in a DBD reactor, Wang et al. [25] identified NH_3* as an effective intermediate species involved in the ammonia to hydrogen conversion at T > 673°C and assumed that this species decomposed through an adsorption/reaction mechanism at surface catalytic sites. This author's assumption relied on the observation of a drastic decay of the NH_3* OES intensity at high temperatures, coinciding with a maximum in the ammonia decomposition yield into N_2 and H_2 [25].

For our experiments without external heating, Figure 6 showcases the evolution with the consumed power of the ammonia decomposition yield and the intensity of the NH* and the NH_3* emission bands for the PZT and Ru-Al_2O_3/PZT reactor configurations. In the two cases, NH* band intensities and decomposition yields followed a similar trend. This similar evolution supports that NH* species are involved in the plasma decomposition of ammonia (note that OES is not quantitative and that only relative values have significance here). Regarding NH_3* bands, it is found that their intensity also increases with power, although at a different pace than the NH* bands (note the different scales in the plots of Figure 6). It is thus noteworthy that, at the highest power, the NH_3*/NH* ratio is less than 1/4 for the PZT configuration (see Figure 6a), while it is around 1/2 for the Ru-Al_2O_3/PZT configuration (see Figure 6b). In other words, there is a comparatively greater concentration of NH_3* species when the PZT pellets are coated with Ru-Al_2O_3, i.e., a reactor configuration rendering the maximum decomposition yield of NH_3. This result contrasts with the said observations of Wang et al. [25] of a sharp decrease in NH_3* species occurring when the decomposition yield of ammonia is maximum, a result attributed to the direct interaction of these intermediate plasma species with surface catalytic sites to render N_2 and H_2 at high temperatures. The different behavior in our experiments where NH_3* species keep a rather constant intensity (c.f., Figure 6b) supports that under the studied reaction conditions at room temperature the decomposition of these species upon adsorption on the Ru-Al_2O_3 coating surface must be negligible with respect to other pure plasma phase decomposition processes. In fact, according to Figure 6b, only at the highest power of 12.5 W there is a small relative decrease in the intensity of NH_3* bands, a feature suggesting an additional but not significant extra decomposition under these conditions.

Unlike other plasma driven reaction processes induced by electron impact, ammonia decomposition does not require very high electron energies. The dissociation energy of the first H-NH_2 bond of the ammonia molecule is 4.7 eV, followed by 4.0 and 3.4 for the H-NH and N-H bonds in NH_2 and NH intermediates, respectively [11]. On the other hand, threshold energies for the following plasma reactions

$$e^- + NH_3 \rightarrow NH + H_2 + e^- \quad (1)$$

$$e^- + NH_3 \rightarrow NH_2 + H + e^- \quad (2)$$

$$e^- + NH_3 \rightarrow NH + 2H + e^- \quad (3)$$

are 4, 5.6 and 8.6 eV respectively [11]. These energy barriers are low in comparison with the dissociation of the N-N bond in the N_2 molecule (i.e., 9.8 eV) [53], a process that has been considered a limiting step for the synthesis of ammonia [51]. We assume that reactions *(1)–(3)* may readily take place in the FBD reactor for the three different configurations. The detection in the plasma of NH* and NH_3* species supports that plasma processes involving electron impact excitation to render NH_3* species or reactions such as those in *(1)–(3)*, followed by dissociation reactions of the formed NH_x* radicals, may account for the ammonia decomposition results obtained here at room temperature. In this regard, the similar evolution of NH* species and decomposition yields (c.f., Figure 6) as a function of power supports that, under our working conditions, ammonia decomposition into H_2 and N_2 is mainly controlled by electron-driven processes. This is further confirmed by the results in Figure 4, indicating that the main experimental parameter controlling reaction efficiency is the current intensity. In

TABLE 1 | Comparison with state-of-the-art results for plasma-assisted ammonia decomposition.

DY-NH_3 [%]	Power [W]	NH_3 Flow rate [sccm]	EE-H_2 (L H_2/kWh)	Comments	Reference
40	12.3	9	25	Planar FBD packed bed reactor with part of the PZT pellets coated with Ru-Al_2O_3. Ambient temperature	This work
99.9	48	120.0	223.8	Cylinder of quartz glass, HVE made of stainless-steel and GE with aluminum foil, 0.5 g 6Fe-4Ni, 500°C and 10 kHz	[27]
17	23	9	6	Packed-bed placed between two parallel stainless-steel electrodes. 25 mA fixed current amplitude. 5 kHz, 2–4 kV	[50]
12	9	5	6	Packed-bed placed between two parallel stainless-steel electrodes. 25 mA fixed current amplitude. 5 kHz, 2–4 kV	[50]
90	45	100	180	The ground electrode (GE) was made of Aluminum foil, the inner high-voltage electrode was a stainless-steel rod. The shell was a quartz tube. The catalyst is Fe-based. 12 kHz	[25]
9.7	34	40	10.3	The reactor temperature increased to 500°C within about 5 min and then kept constant with input power of 26 W, discharge frequency 12 kHz. Cheap Fe-based catalyst in its discharge zone.	[24]
100	30	40	119	The reactor temperature increased to 500°C within about 5 min and then kept constant with input power 26 W, discharge frequency 12 kHz. Cheap Fe-based catalyst in its discharge zone.	[24]
5	21	75	16.1	A coaxial packed-bed DBD reactor of quartz was used. The outer electrode was a stainless-steel mesh tightly wrapped; the inner electrode was a stainless-steel rod. The decomposition of NH_3 was carried at 21 W, a frequency of 3.0 kHz and 4.5 mm gap.	[29]
13	21	75	41.8	A coaxial packed-bed DBD reactor of quartz was used. The outer electrode was a stainless-steel mesh tightly wrapped; the inner electrode was a stainless-steel rod. The decomposition of NH_3 was carried at 21 W, a frequency of 3.0 kHz and 4.5 mm gap.	[29]
14	10.7	4.5	10.4	Packed-bed reactor filled with $BaTiO_3$ pellets. Atmospheric pressure and room temperature. No catalyst.	[61]
11	11.4	9	7.5	Packed-bed reactor filled with $BaTiO_3$ pellets. Atmospheric pressure and room temperature. No catalyst.	[61]
8.4	3.8	25	49.5	Packed-bed reactor filled with $BaTiO_3$ pellets. Atmospheric pressure and room temperature. No catalyst.	[61]
3.5	0.51	25	150	Packed-bed reactor filled with $BaTiO_3$ pellets. Atmospheric pressure and room temperature. No catalyst.	[61]

agreement with previously reported COMSOL Multiphysics® simulation studies about the ammonia synthesis reaction [35], we deem that coating the PZT pellets with Al_2O_3, a material characterized by a much lower permittivity than PZT, will reduce the total current intensity and be the cause of the observed decrease in reaction yield. In the same line of reasoning, we assume that the incorporation of a Ru-Al_2O_3 coating, characterized by an effective higher permittivity as demonstrated by our analysis in Figure 3d, is the key factor responsible for the observed increase in reaction yield [54]. The COMSOL Multiphysics® simulations in Figure 2 effectively confirms that increasing the permittivity of the coating, as expected for an metal-alumina effective medium, produces an enhancement in the plasma density among pellets.

The considerations above support an effective control of reactor performance (i.e., yield and efficiency) by the electrical characteristics of the FBD reactor depending on the electrical permittivity of the material incorporated into the pellets. However, this does not necessarily discount second order contributions [54–56], such as the emission of high-energy electrons by the metal particles at the surface as proposed by Kushner and collaborators [57], and/or a marginal involvement of Eley-Rideal and/or Langmuir-Hinshelwood processes at the surface of the modified pellets [58]. In this regard, XPS analysis of the used Ru-Al_2O_3/PZT pellets provided some hints of a possible interaction of ruthenium nanoparticles with ammonia species. An inconclusive evidence in this regard was a small shoulder at around 397-398 eV (i.e., the region where N1s peaks appear) that is compatible with the formation of surface metal nitride bonds (see spectra in Supplementary Material S7) [59].

3.4 | Comparison with State-of-The-Art Results

The high reaction yields obtained in this study compare well with recently published results obtained with packed-bed reactors and hydrogen selective membrane plasma systems working at high temperatures or with mixtures of ammonia and other gasses [28, 60]. In Table 1 we gather data from other studies in comparison with the herein reported results [24, 25, 27, 29, 50, 61]. Most studies in literature with packed bed DBD reactors use catalysts and operate at high temperatures. The promising 40% decomposition yield obtained here with pure ammonia at atmospheric pressure and room temperature proves the high efficiency of FBD plasmas. We think that new approaches based on ferroelectric packed-bed reactors applying effective medium concepts—based on metal/dielectric layers to further enhance total current in the reactors—constitute a promising strategy to enhance reactivity and to leverage the development of alternative pure-ammonia decomposition processes of practical interest.

4 | Conclusions

The *ammonia to hydrogen* process has been studied in a modified ferroelectrically moderated packed-bed plasma reactor working at room temperature and atmospheric pressure. Three different barrier configurations have been used to properly assess the effect on process performance of the incorporation onto the packed-bed of metal nanoparticles with potential catalytic effects. Our results show a higher percentage of ammonia decomposition when metal ruthenium nanoparticles are incorporated into an alumina coating. The obtained results reveal an increase in current intensity and electron density due to the inclusion of the Ru metal particles, the latter attributed to a higher dielectric permittivity of the barrier, as expected from considerations based on effective medium concepts. The collected findings support those catalytic effects, if present, are second order and that most processes leading to NH_3 decomposition occur in the plasma (gas) phase. Conclusively, under the conditions studied, the incorporation of a metal-dielectric coating has a more significant impact on the electrical properties of a FBD plasma reactor than possible catalytic interactions. Our findings support the use of effective medium materials as an alternative concept to describe the modifications occurring in the plasma when metal-oxide coatings are added to the barrier of packed-bed plasma reactors.

Acknowledgments

This study was supported by projects PID2020-114270RA-I00, PID2020-112620GB-I00 and PID2023-147916NA-I00 funded by MCIN/AEI/10.13039/501100011033, project TED2021-130124A-I00 funded by AEI/10.13039/501100011033/Unión Europea Next Generation EU/PRTR and projects US-1381045, and US-1380977 funded by Conserjería de Economía, Conocimiento, Empresas and Universidad de la Junta de Andalucía (PAIDI-2020) and Programa Operativo Feder 2014-2020. The authors would like to thank F. Vattier from the Materials Science Institute of Sevilla for the XPS measurements and J. Gil-Rostra for his support with impedance measurements.

Conflicts of Interest

The authors declare no conflicts of interest.

Data Availability Statement

The data that support the findings of this study are available from the corresponding author upon reasonable request.

References

1. C. Smith, A. K. Hill, and L. Torrente-Murciano, "Current and Future Role of Haber-Bosch Ammonia in a Carbon-Free Energy Landscape," *Energy and Environmental Science* 13 (2020): 331–344, https://doi.org/10.1039/c9ee02873k.

2. S. F. Yin, Q. H. Zhang, B. Q. Xu, W. X. Zhu, C. F. Ng, and C. T. Au, "Investigation on the Catalysis of COx-Free Hydrogen Generation From Ammonia," *Journal of Catalysis* 224 (2004): 384–396, https://doi.org/10.1016/J.JCAT.2004.03.008.

3. I. Lucentini, X. Garcia, X. Vendrell, and J. Llorca, "Review of the Decomposition of Ammonia to Generate Hydrogen," *Industrial and Engineering Chemistry Research* 60 (2021): 18560–18611, https://doi.org/10.1021/acs.iecr.1c00843.

4. M. Pinzón, E. Ruiz-López, A. Romero, A. R. de la Osa, P. Sánchez, and A. de Lucas-Consuegra, "Electrochemical Activation of Ru Catalyst With Alkaline Ion Conductors for the Catalytic Decomposition of Ammonia," *Molecular Catalysis* 511 (2021): 111721, https://doi.org/10.1016/J.MCAT.2021.111721.

5. J. C. Devins and M. Burton, "Formation of Hydrazine in Electric Discharge Decomposition of Ammonia," *Journal of the American Chemical Society* 76 (2002): 2618–2626, https://doi.org/10.1021/JA01639A006.

6. R. D'agostino, F. Cramarossa, S. D. Benedictis, and G. Ferraro, "Kinetic and Spectroscopic Analysis of NH_3 Decomposition Under R.F. Plasma at Moderate Pressures," *Plasma Chemistry and Plasma Processing* 1 (1981): 19–35.

7. J. E. Nicholas, A. I. Spiers, and N. A. Martin, "Kinetics and Mechanism in the Decomposition of NH_3 in a Radio-Frequency Pulse Discharge," *Plasma Chemistry and Plasma Processing* 6 (1986): 39–51.

8. M. Akiyama, K. Aihara, T. Sawaguchi, M. Matsukata, and M. Iwamoto, "Ammonia Decomposition to Clean Hydrogen Using Non-Thermal Atmospheric-Pressure Plasma," *International Journal of Hydrogen Energy* 43 (2018): 14493–14497, https://doi.org/10.1016/j.ijhydene.2018.06.022.

9. F. Gorky, A. Best, J. Jasinski, B. J. Allen, A. C. Alba-Rubio, and M. L. Carreon, "Plasma Catalytic Ammonia Synthesis on Ni Nanoparticles: The Size Effect," *Journal of Catalysis* 393 (2021): 369–380, https://doi.org/10.1016/j.jcat.2020.11.030.

10. F. Gorky, J. M. Lucero, J. M. Crawford, et al., "Insights on Cold Plasma Ammonia Synthesis and Decomposition Using Alkaline Earth Metal-Based Perovskites," *Catalysis: Science and Technology* 11 (2021): 5109–5118, https://doi.org/10.1039/d1cy00729g.

11. Y. Yi, L. Wang, and H. Guo, "Plasma-Catalytic Decomposition of Ammonia for Hydrogen Energy." in *Plasma Catalysis. Fundamentals and Applications*, eds. X. Tu, J. C. Whitehead, and T. Nozaki (Cham: Springer, 2019). 1st ed., 181–230, https://doi.org/10.1007/978-3-030-05189-1_7.

12. K. H. Lim, Y. Yue, N. Bella, et al., "Sustainable Hydrogen and Ammonia Technologies With Nonthermal Plasma Catalysis: Mechanistic Insights and Technoeconomic Analysis," *ACS Sustainable Chemistry and Engineering* 11 (2023): 4903–4933, https://doi.org/10.1021/ACSSUSCHEMENG.2C06515/ASSET/IMAGES/MEDIUM/SC2C06515_0023.GIF.

13. X. Huang, K. Lei, Y. Mi, W. Fang, and X. Li, "Recent Progress on Hydrogen Production From Ammonia Decomposition: Technical Roadmap and Catalytic Mechanism," *Molecules (Basel, Switzerland)* 28 (2023): 5245 28, https://doi.org/10.3390/MOLECULES28135245.

14. S. Bang, R. Snoeckx, and M. S. Cha, "Kinetic Study for Plasma Assisted Cracking of NH_3: Approaches and Challenges," *Journal of Physical Chemistry A* 127 (2023): 1271–1282, https://doi.org/10.1021/ACS.JPCA.2C06919/SUPPL_FILE/JP2C06919_SI_002.ZIP.

15. Y. Gorbanev, I. Fedirchyk, and A. Bogaerts, "Plasma Catalysis in Ammonia Production and Decomposition: Use It, or Lose It?," *Current Opinion in Green and Sustainable Chemistry* 47 (2024): 100916, https://doi.org/10.1016/j.cogsc.2024.100916.

16. R. C. Seyfeli and D. Varisli, "Ammonia Decomposition Reaction to Produce COx-Free Hydrogen Using Carbon Supported Cobalt Catalysts in Microwave Heated Reactor System," *International Journal of Hydrogen Energy* 45 (2020): 34867–34878, https://doi.org/10.1016/j.ijhydene.2020.01.124.

17. M. Akca and D. Varisli, "Performance of Co-Fe@Alumina Catalysts in Comparison to Monometallic Co@Alumina and Fe@Alumina Catalysts for Microwave Assisted COx-Free Hydrogen Production," *Molecular Catalysis* 485 (2020): 110823, https://doi.org/10.1016/j.mcat.2020.110823.

18. M. Awaji, L. Pentecoste-Cuynet, C. Noël, T. Gries, M. Belmahi, and T. Belmonte, "Ammonia Cracking by Microwave Plasma under Reduced Pressure," *International Journal of Hydrogen Energy* 119 (2025): 377–385, https://doi.org/10.1016/j.ijhydene.2025.03.118.

19. M. Młotek, M. Perron, and K. Krawczyk, "Ammonia Decomposition in a Gliding Discharge Plasma," *Energy Technology* 9 (2021): 2100677, https://doi.org/10.1002/ente.202100677.

20. Y. Zhao, L. Wang, J. Zhang, and H. Guo, "Enhancing the Ammonia to Hydrogen (ATH) Energy Efficiency of Alternating Current Arc Discharge," *International Journal of Hydrogen Energy* 39 (2014): 7655–7663, https://doi.org/10.1016/j.ijhydene.2014.03.128.

21. Y. Zhao, L. Wang, J. Zhang, W. Gong, and H. Guo, "Decomposition of Ammonia by Atmospheric Pressure AC Discharge: Catalytic Effect of the Electrodes," *Catalysis Today* 211 (2013): 72–77, https://doi.org/10.1016/j.cattod.2013.03.027.

22. Q. F. Lin, Y. M. Jiang, C. Z. Liu, et al., "Instantaneous Hydrogen Production From Ammonia by Non-Thermal Arc Plasma Combining With Catalyst," *Energy Reports* 7 (2021): 4064–4070, https://doi.org/10.1016/j.egyr.2021.06.087.

23. L. Wang, Y. Yi, Y. Zhao, R. Zhang, J. Zhang, and H. Guo, "NH_3 Decomposition for H_2 Generation: Effects of Cheap Metals and Supports on Plasma-Catalyst Synergy," *ACS Catalysis* 5 (2015): 4167–4174, https://doi.org/10.1021/acscatal.5b00728.

24. L. Wang, Y. Zhao, C. Liu, W. Gong, and H. Guo, "Plasma Driven Ammonia Decomposition on a Fe-Catalyst: Eliminating Surface Nitrogen Poisoning," *Chemical communications (Cambridge, England)* 49 (2013): 3787–3789, https://doi.org/10.1039/c3cc41301b.

25. L. Wang, Y. Yi, Y. Guo, Y. Zhao, J. Zhang, and H. Guo, "Synergy of DBD Plasma and Fe-Based Catalyst in NH3 Decomposition: Plasma Enhancing Adsorption Step," *Plasma Processes and Polymers* 14 (2017): 1600111, https://doi.org/10.1002/ppap.201600111.

26. L. Wang, Y. H. Yi, H. C. Guo, X. M. Du, B. Zhu, and Y. M. Zhu, "Highly Dispersed Co Nanoparticles Prepared by An Improved Method for Plasma-Driven NH_3 Decomposition to Produce H_2," *Catalysts* 9 (2019): 107, https://doi.org/10.3390/catal9020107.

27. Y. Yi, L. Wang, Y. Guo, S. Sun, and H. Guo, "Plasma-Assisted Ammonia Decomposition over Fe–Ni Alloy Catalysts for COx-Free Hydrogen," *AIChE Journal* 65 (2019): 691–701, https://doi.org/10.1002/aic.16479.

28. Y. Hayakawa, S. Kambara, and T. Miura, "Hydrogen Production From Ammonia by the Plasma Membrane Reactor," *International Journal of Hydrogen Energy* 45 (2020): 32082–32088, https://doi.org/10.1016/j.ijhydene.2020.08.178.

29. J. A. Andersen, J. M. Christensen, M. Østberg, A. Bogaerts, and A. D. Jensen, "Plasma-Catalytic Ammonia Decomposition Using a Packed-Bed Dielectric Barrier Discharge Reactor," *International Journal of Hydrogen Energy* 47 (2022): 32081–32091, https://doi.org/10.1016/J.IJHYDENE.2022.07.102.

30. M. El-Shafie, S. Kambara, and Y. Hayakawa, "Plasma-Enhanced Catalytic Ammonia Decomposition over Ruthenium (Ru/Al_2O_3) and Soda Glass (SiO_2) Materials," *Journal of the Energy Institute* 99 (2021): 145–153, https://doi.org/10.1016/J.JOEI.2021.09.001.

31. Y. Gao, E. Hu, Y. Yi, G. Yin, and Z. Huang, "Plasma-Assisted Low Temperature Ammonia Decomposition on 3d Transition Metal (Fe, Co and Ni) Doped CeO_2 Catalysts: Synergetic Effect of Morphology and Co-Doping," *Fuel Processing Technology* 244 (2023): 107695, https://doi.org/10.1016/J.FUPROC.2023.107695.

32. A. Gómez-Ramírez, R. Álvarez, P. Navascués, et al., "Electrical and Reaction Performances of Packed-Bed Plasma Reactors Moderated With Ferroelectric or Dielectric Materials," *Plasma Processes and Polymers* 18 (2021): 2000193, https://doi.org/10.1002/ppap.202000193.

33. A. Gómez-Ramírez, J. Cotrino, R. M. Lambert, and A. R. González-Elipe, "Efficient Synthesis of Ammonia From N_2 and H_2 Alone in a Ferroelectric Packed-Bed DBD Reactor," *Plasma Sources Science and Technology* 24 (2015): 065011, https://doi.org/10.1088/0963-0252/24/6/065011.

34. J. Liu, X. Zhu, S. Jiang, et al., "Plasma-Catalytic Synthesis of Ammonia over $Ru/BaTiO_3$-based Bimetallic Catalysts: Synergistic Effect From Dual-Metal Active Sites," *Fuel Processing Technology* 250 (2023): 107851, https://doi.org/10.1016/j.fuproc.2023.107851.

35. P. Navascués, J. Garrido-García, J. Cotrino, A. R. González-Elipe, and A. Gómez-Ramírez, "Incorporation of a Metal Catalyst for the Ammonia Synthesis in a Ferroelectric Packed-Bed Plasma Reactor: Does It Really Matter?," *ACS sustainable chemistry & engineering* 11 (2023): 3621–3632, https://doi.org/10.1021/acssuschemeng.2c05877.

36. A. V. Pipa and R. Brandenburg, "The Equivalent Circuit Approach for the Electrical Diagnostics of Dielectric Barrier Discharges: The Classical Theory and Recent Developments," *Atoms* 7 (2019): 14, https://doi.org/10.3390/atoms7010014.

37. A. M. Montoro-Damas, J. J. Brey, M. A. Rodríguez, A. R. González-Elipe, and J. Cotrino, "Plasma Reforming of Methane in a Tunable Ferroelectric Packed-Bed Dielectric Barrier Discharge Reactor," *Journal of Power Sources* 296 (2015): 268–275, https://doi.org/10.1016/j.jpowsour.2015.07.038.

38. COMSOL AB., COMSOL Multiphysics® v. 6.0, Stockholm, Sweden, www.comsol.com.

39. COMSOL AB., COMSOL Documentation: Plasma Module - Dirent Current Discharges - Dielectric Barrier Discharge, www.comsol.com.

40. COMSOL AB., COMSOL Documentation: Plasma Module - Capacitively Coupled Plasmas - Alpha to Gamma Transition, www.comsol.com.

41. Z. Shi, S. Chen, R. Fan, et al., "Ultra Low Percolation Threshold and Significantly Enhanced Permittivity in Porous Metal–Ceramic Composites," *Journal of Materials Chemistry* C 2 (2014): 6752–6757, https://doi.org/10.1039/C4TC01117A.

42. H. Du, X. Lin, H. Zheng, B. Qu, Y. Huang, and D. Chu, "Colossal Permittivity in Percolative Ceramic/Metal Dielectric Composites," *Journal of Alloys and Compounds* 663 (2016): 848–861, https://doi.org/10.1016/J.JALLCOM.2015.12.171.

43. J. Huang, H. Zheng, Z. Chen, Q. Gao, N. Ma, and P. Du, "Percolative Ceramic Composites With Giant Dielectric Constants and Low Dielectric Losses," *Journal of Materials Chemistry* 19, (2009): 3909–3913, https://doi.org/10.1039/B820815H.

44. I. Comsol, Dielectric Barrier Discharge, version 6.2, (n.d.), www.comsol.com.

45. C. D. Bie, "Fluid Modeling of the Plasma-Assisted Conversion of Greenhouse Gases to Value-Added Chemicals in a Dielectric Barrier Discharge," (2016).

46. K. V. Laer and A. Bogaerts, "How Bead Size and Dielectric Constant Affect the Plasma Behaviour in a Packed Bed Plasma Reactor: A Modelling Study," *Plasma Sources Science and Technology* 26 (2017): 085007, https://doi.org/10.1088/1361-6595/aa7c59.

47. B. Loenders, R. Michiels, and A. Bogaerts, "Is a Catalyst Always Beneficial in Plasma Catalysis? Insights From the Many Physical and Chemical Interactions," *Journal of Energy Chemistry* 85 (2023): 501–533, https://doi.org/10.1016/j.jechem.2023.06.016.

48. R. De Meyer, Y. Gorbanev, R.-G. Ciocarlan, P. Cool, S. Bals, and A. Bogaerts, "Importance of Plasma Discharge Characteristics in Plasma Catalysis: Dry Reforming of Methane vs. Ammonia Synthesis," *Chemical Engineering Journal* 488 (2024): 150838, https://doi.org/10.1016/j.cej.2024.150838.

49. T.-W. Liu, F. Gorky, M. L. Carreon, and D. A. Gómez-Gualdrón, "Energetics of Reaction Pathways Enabled by N and H Radicals During Catalytic, Plasma-Assisted NH_3 Synthesis," *ACS Sustainable Chemistry & Engineering* 10 (2022): 2034–2051, https://doi.org/10.1021/acssuschemeng.1c05660.

50. P. Navascués, J. M. Obrero-Pérez, J. Cotrino, A. R. González-Elipe, and A. Gómez-Ramírez, "Unraveling Discharge and Surface Mechanisms in Plasma-Assisted Ammonia Reactions," *ACS Sustainable Chemistry & Engineering* 8 (2020): 14855–14866, https://doi.org/10.1021/ACSSUSCHEMENG.0C04461.

51. A. Gómez-Ramírez, A. M. Montoro-Damas, J. Cotrino, R. M. Lambert, and A. R. González-Elipe, "About the Enhancement of Chemical Yield During the Atmospheric Plasma Synthesis of Ammonia in a Ferroelectric Packed Bed Reactor," *Plasma Processes and Polymers* 14 (2017): 1600081, https://doi.org/10.1002/ppap.201600081.

52. R. W. B. Pearse and A. G. Gaydon, *The Identification of Molecular Spectra* (Chapman & Hall, 1965). 3rd ed..

53. "The Dissociation Energy of the Nitrogen Molecule," *Proceedings of the Royal Society of London, Series A. Mathematical and Physical Sciences* 236 (1956): 278–284, https://doi.org/10.1098/RSPA.1956.0135.

54. C. Ndayirinde, Y. Gorbanev, R.-G. Ciocarlan, et al., "Plasma-Catalytic Ammonia Synthesis: Packed Catalysts Act as Plasma Modifiers," *Catalysis Today* 419 (2023): 114156, https://doi.org/10.1016/j.cattod.2023.114156.

55. M. Ruiz-Martín, M. Oliva-Ramírez, A. R. González-Elipe, and A. Gómez-Ramírez, "Plasma Catalysis for Gas Conversion – Impact of Catalyst on the Plasma Behavior," *Current Opinion in Green and Sustainable Chemistry* 51 (2025): 100990, https://doi.org/10.1016/j.cogsc.2024.100990.

56. R. Cimerman, M. Cíbiková, L. Satrapinskyy, and K. Hensel, "The Effect of Packing Material Properties on Tars Removal by Plasma Catalysis," *Catalysts* 10 (2020): 1476, https://doi.org/10.3390/catal10121476.

57. J. Kruszelnicki, K. W. Engeling, J. E. Foster, and M. J. Kushner, "Interactions Between Atmospheric Pressure Plasmas and Metallic Catalyst Particles in Packed Bed Reactors," *Journal of Physics D: Applied Physics* 54 (2020): 104001, https://doi.org/10.1088/1361-6463/ABCC92.

58. M. L. Carreon, "Plasma Catalysis: A Brief Tutorial," *Plasma Research Express* 1 (2019): 043001, https://doi.org/10.1088/2516-1067/ab5a30.

59. M. G. Moreno-Armenta, J. Diaz, A. Martinez-Ruiz, and G. Soto, "Synthesis of Cubic Ruthenium Nitride by Reactive Pulsed Laser Ablation," *Journal of Physics and Chemistry of Solids* 68 (2007): 1989–1994, https://doi.org/10.1016/j.jpcs.2007.06.002.

60. Y. Hayakawa, T. Miura, K. Shizuya, S. Wakazono, K. Tokunaga, and S. Kambara, "Hydrogen Production System Combined With a Catalytic Reactor and a Plasma Membrane Reactor From Ammonia," *International Journal of Hydrogen Energy* 44 (2019): 9987–9993, https://doi.org/10.1016/j.ijhydene.2018.12.141.

61. M. Ruiz-Martín, S. Marín-Meana, A. Megías-Sánchez, et al., "H_2 Production From NH_3 in a $BaTiO_3$ Moderated Ferroelectric Packed-Bed Plasma Reactor," *Plasma Chemistry and Plasma Processing* 43 (2023): 2093–2110, https://doi.org/10.1007/s11090-023-10427-7.

Supporting Information

Additional supporting information can be found online in the Supporting Information section.

Appendix A: Questionnaire/Interview script The Supplementary Material includes the following information: S1 - Alumina-supported ruthenium (Ru) catalyst preparation procedure, S2 - Stability analysis and voltage dependence in the COMSOL simulations, S3 - Impedance spectroscopy analysis of the packed-bed reactor with different barriers, S4 - Equivalent circuit model, S5 - QMS spectra before and after plasma ignition for pure-ammonia discharges, S6 – Comparison of OES spectra for the three barrier configurations, S7 - XPS analysis of the Ru-Al_2O_3/PZT pellets before and after plasma exposure.